Supporting information

Enhanced Electrical, Thermal and Mechanical Properties of SnTe

through Equi-Molar Multi-Cation Alloying for Suitable Device

Applications

Samuel Kimani Kihoi,^a U Sandhya Shenoy,^b Hyunji Kim,^a Joseph Ngugi Kahiu,^a Cheol Min

Kim, a Kwi-Il Park, a Denthaje Krishna Bhat, c Ho Seong Lee a,*

^aDepartment of Materials Science and Metallurgical Engineering, Kyungpook National

University, 80 Daehak-ro, Buk-gu, Daegu, 41566, Republic of Korea

^bDepartment of Materials Science and Engineering, Institute of Engineering and Technology,

Srinivas University, Mukka -574146, Mangalore, Karnataka, India

^cDepartment of Chemistry, National Institute of Technology Karnataka, Surathkal,

Srinivasnagar -575025, Mangalore, Karnataka, India

E-mail: hs.lee@knu.ac.kr

S1

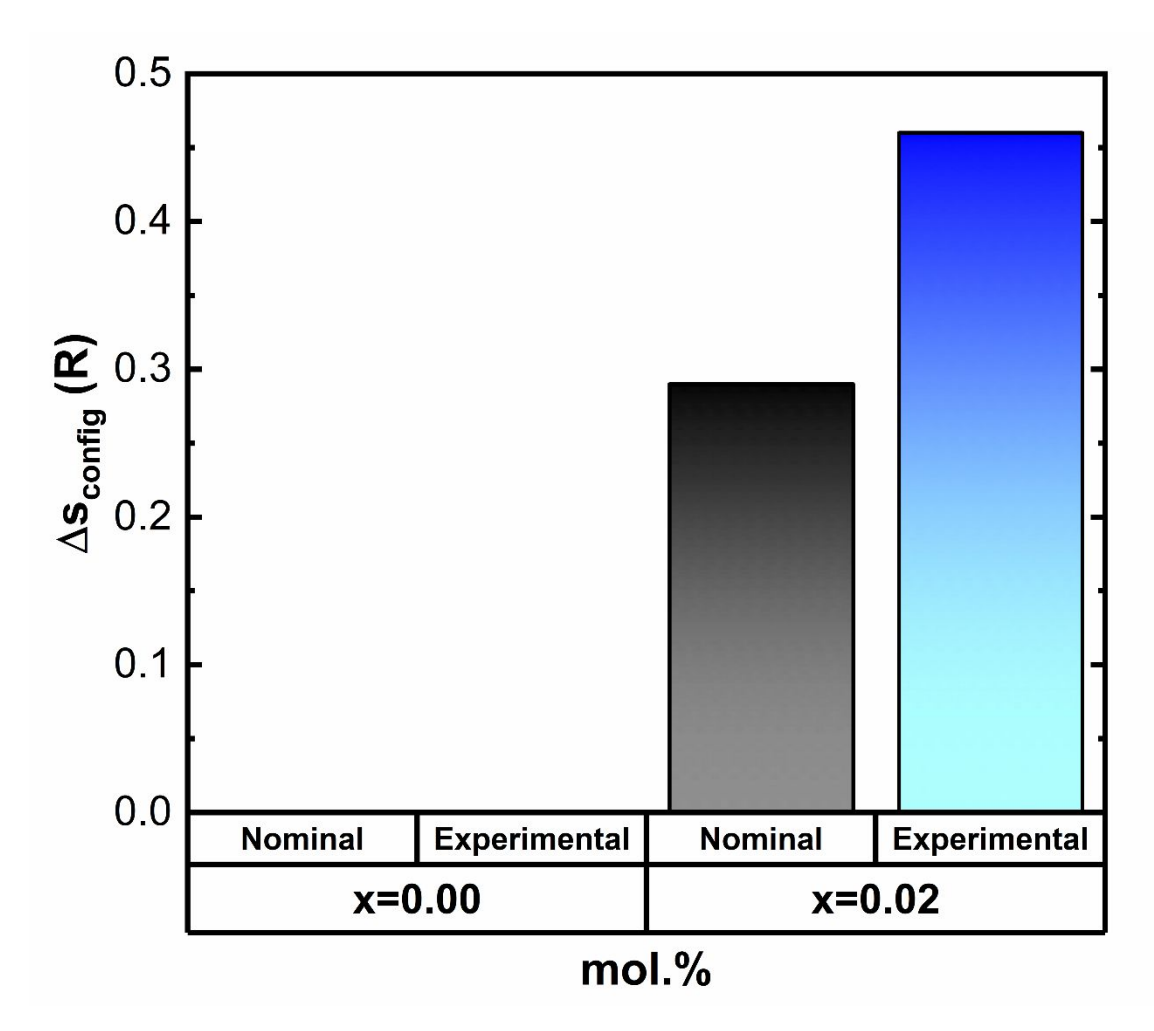


Figure S1. Calculated configurational entropy of the x=0.00 and x=0.02 compositions. Nominal composition is from the respective stoichiometric concentration whereas experimental composition is from the EPMA's matrix composition.

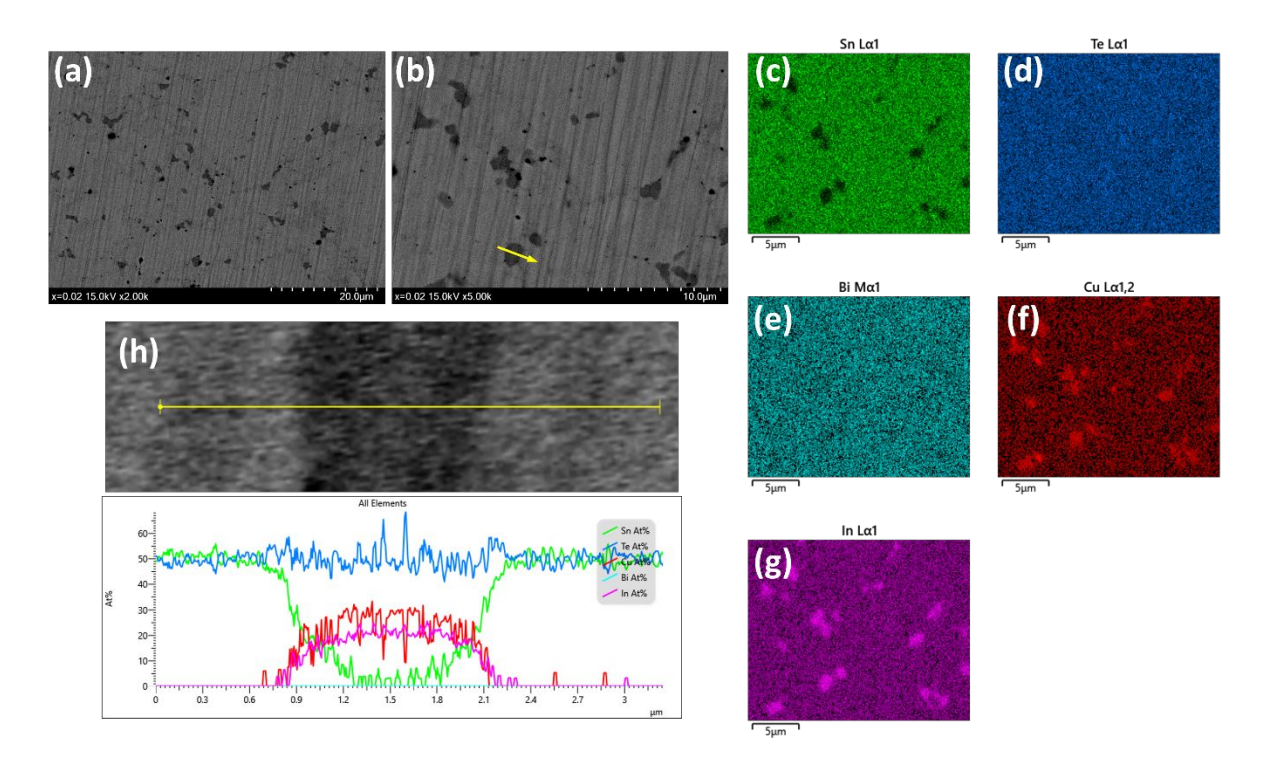


Figure S2. (a) Low and (b) high magnification SEM BSE images, (c-g) corresponding EDS elemental mapping for the x=0.02 composition of (b) and (h) line scan data along the yellow arrow showing the composition of the CuInTe₂ ternary phase within the matrix for the x=0.02 composition.

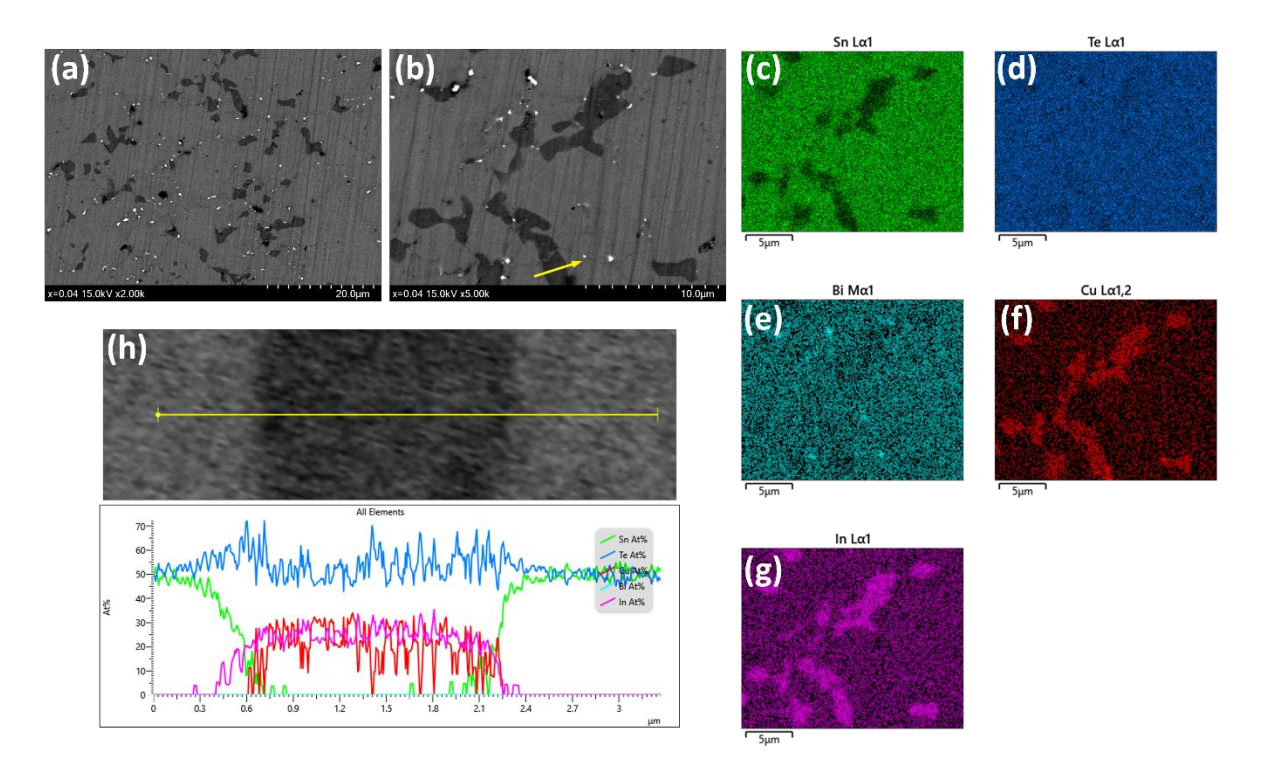


Figure S3. (a) Low and (b) high magnification SEM BSE images, (c-g) corresponding EDS elemental mapping for the x=0.02 composition of (b) and (h) line scan data along the yellow arrow showing the composition of the CuInTe₂ ternary phase within the matrix for the x=0.04 composition.

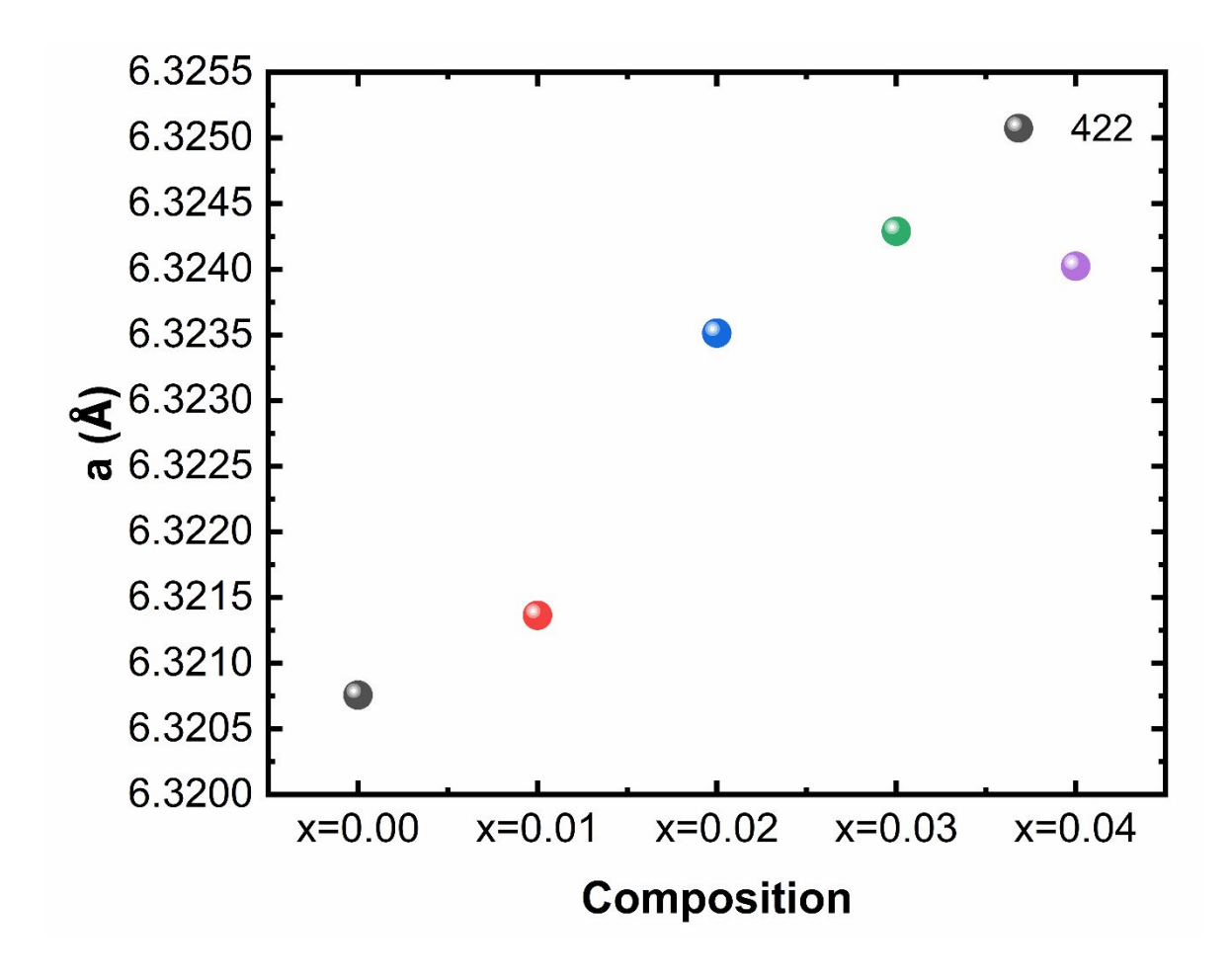


Figure S4. Calculated lattice parameter for the Sn_{1-3x}Bi_xCu_xIn_xTe compositions.

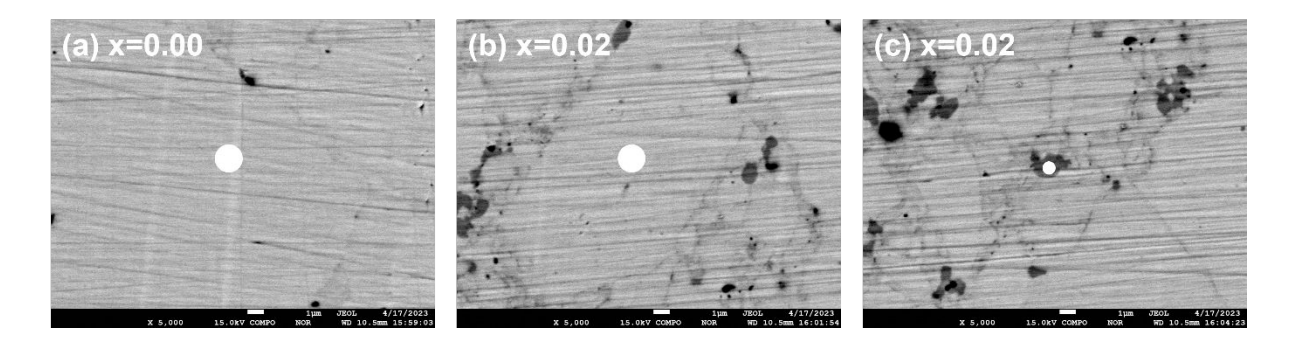


Figure S5. BSE images from EPMA for the compositions (a) x=0.00 at the matrix and (b, c) x=0.02 at the matrix and second phase, respectively. The white spots shows where the composition analysis was done.

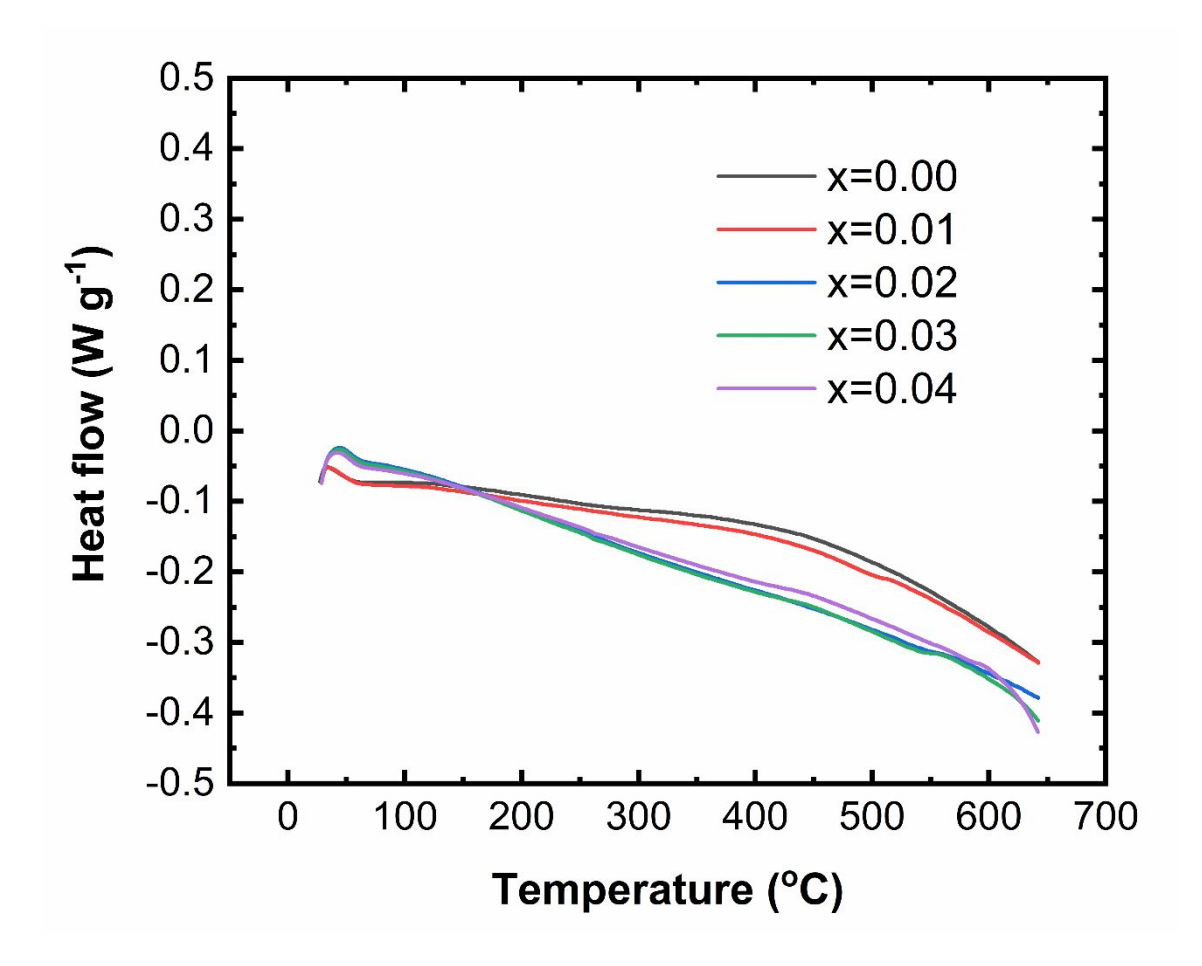


Figure S6. DSC profiles for the Sn_{1-3x}Bi_xCu_xIn_xTe compositions.

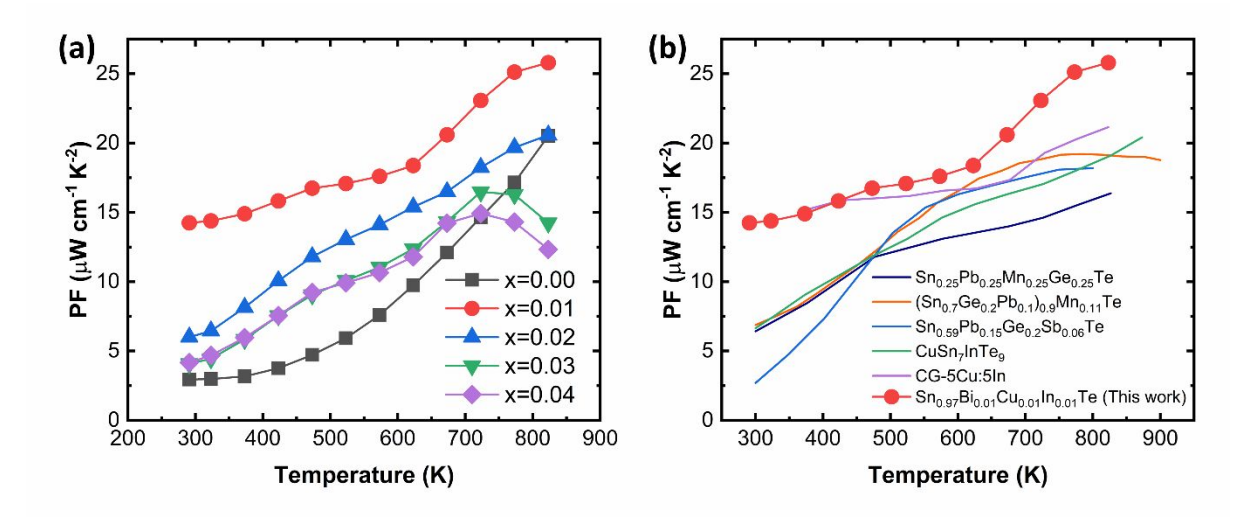


Figure S7. Figure. (a) Temperature-dependent power factor, PF for the $Sn_{1-3x}Bi_xCu_xIn_xTe$ compositions. (b) Comparison of the maximum power factor of the EMMCA low entropy x=0.01 composition in this work with other high entropy alloys with an equivalent number of elements including $Sn_{0.25}Pb_{0.25}Mn_{0.25}Ge_{0.25}Te$, $(Sn_{0.7}Ge_{0.2}Pb_{0.1})_{0.9}Mn_{0.11}Te$, and $Sn_{0.59}Pb_{0.15}Ge_{0.2}Sb_{0.06}Te$, $CuSn_7InTe_9$ composite, $CuSn_7InTe_9$ and $CuInTe_2/SnTe$ coated grain nanocomposite (CG-5Cu:5In).

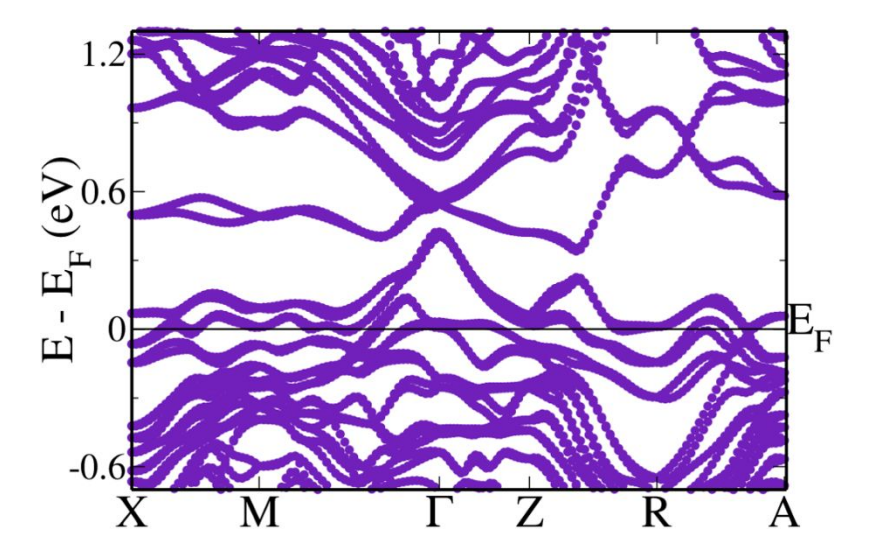


Figure S8. Electronic structure of Sn₁₂BiInCuTe₁₆.

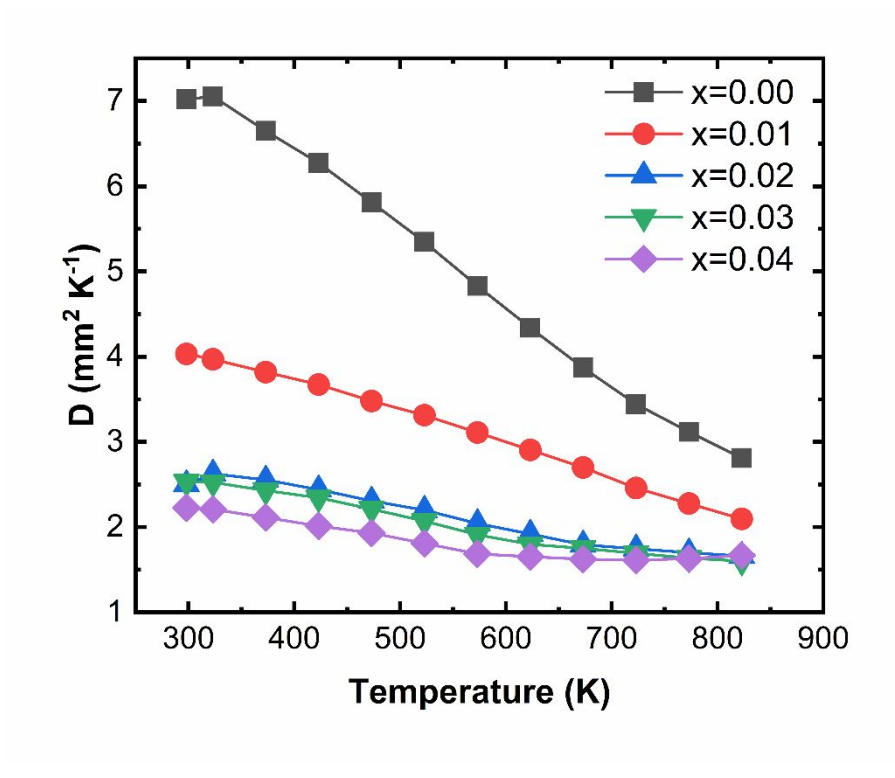


Figure S9. Temperature-dependent thermal diffusivity for the Sn_{1-3x}Bi_xCu_xIn_xTe compositions.

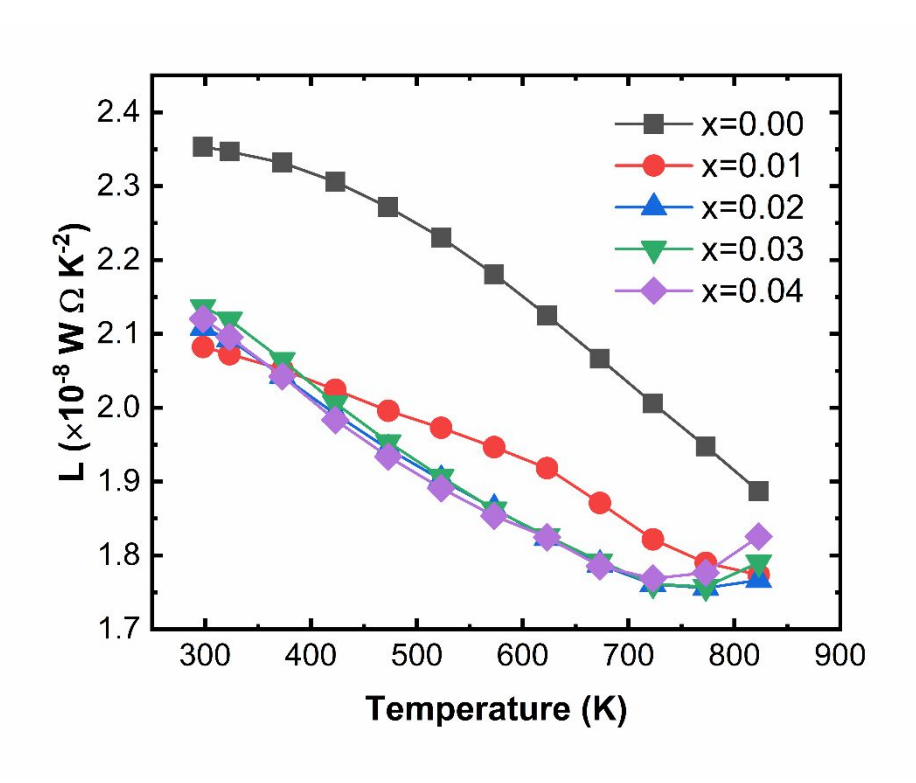


Figure S10. Temperature-dependent Lorenz number for the Sn_{1-3x}Bi_xCu_xIn_xTe compositions.

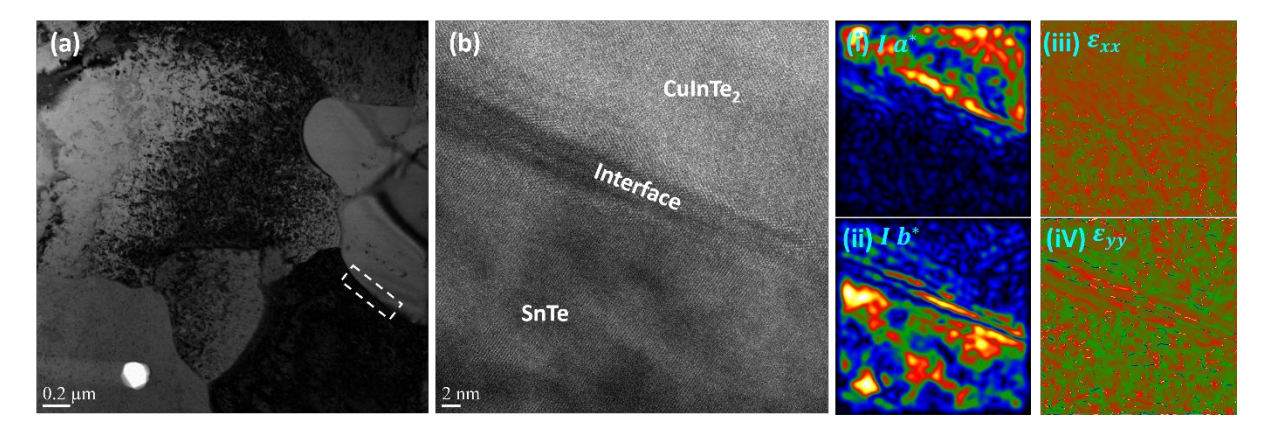


Figure S11. (a) BF image (b) HRTEM image obtained at the interface between the SnTe matrix and the CuInTe₂ precipitate. (i & ii) corresponding intensity and (iii & IV) strain tensor maps obtained using geometric phase analysis (GPA)⁶ of (b).

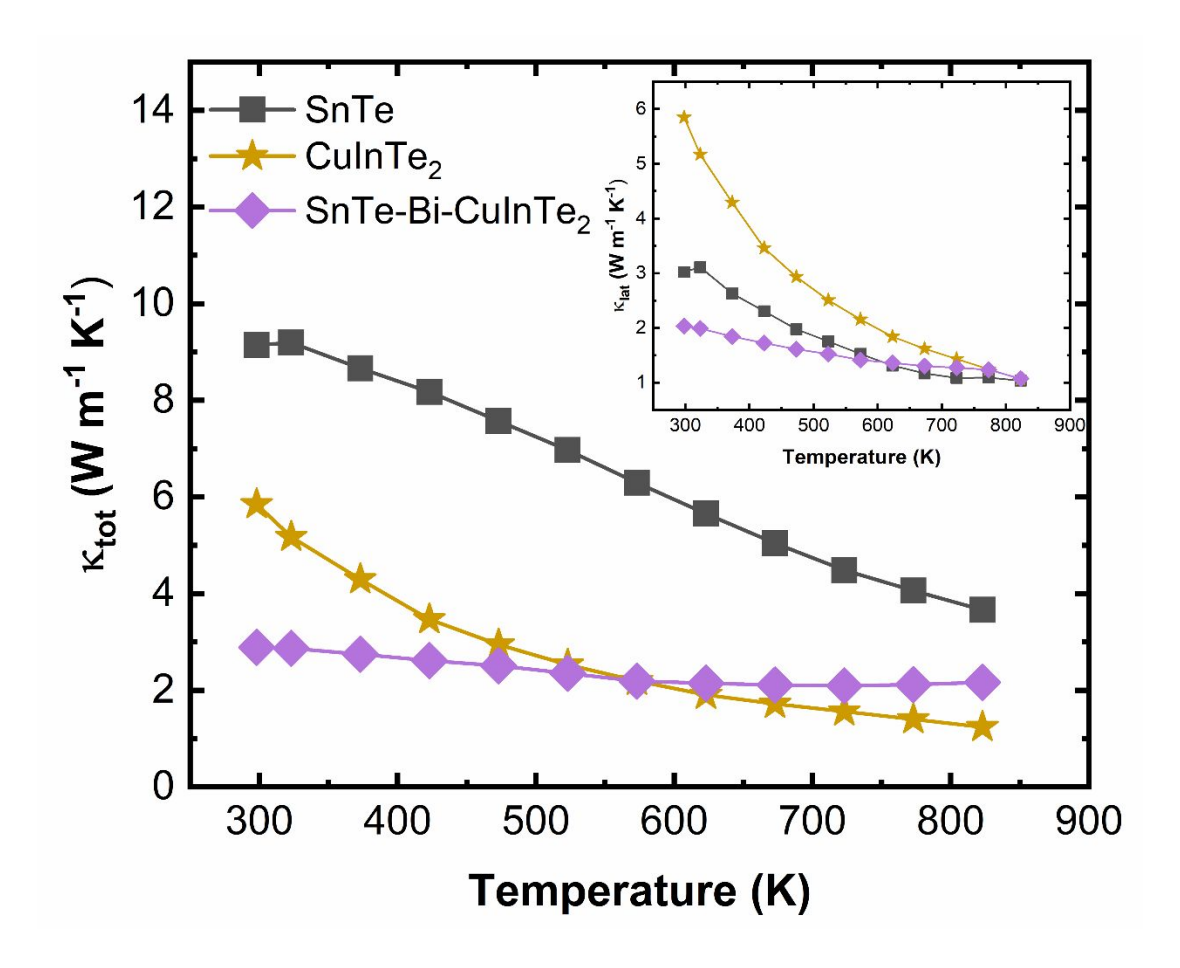


Figure S12. Comparison of the thermal conductivity of this work and $CuInTe_2$ ⁷ from our previous study.

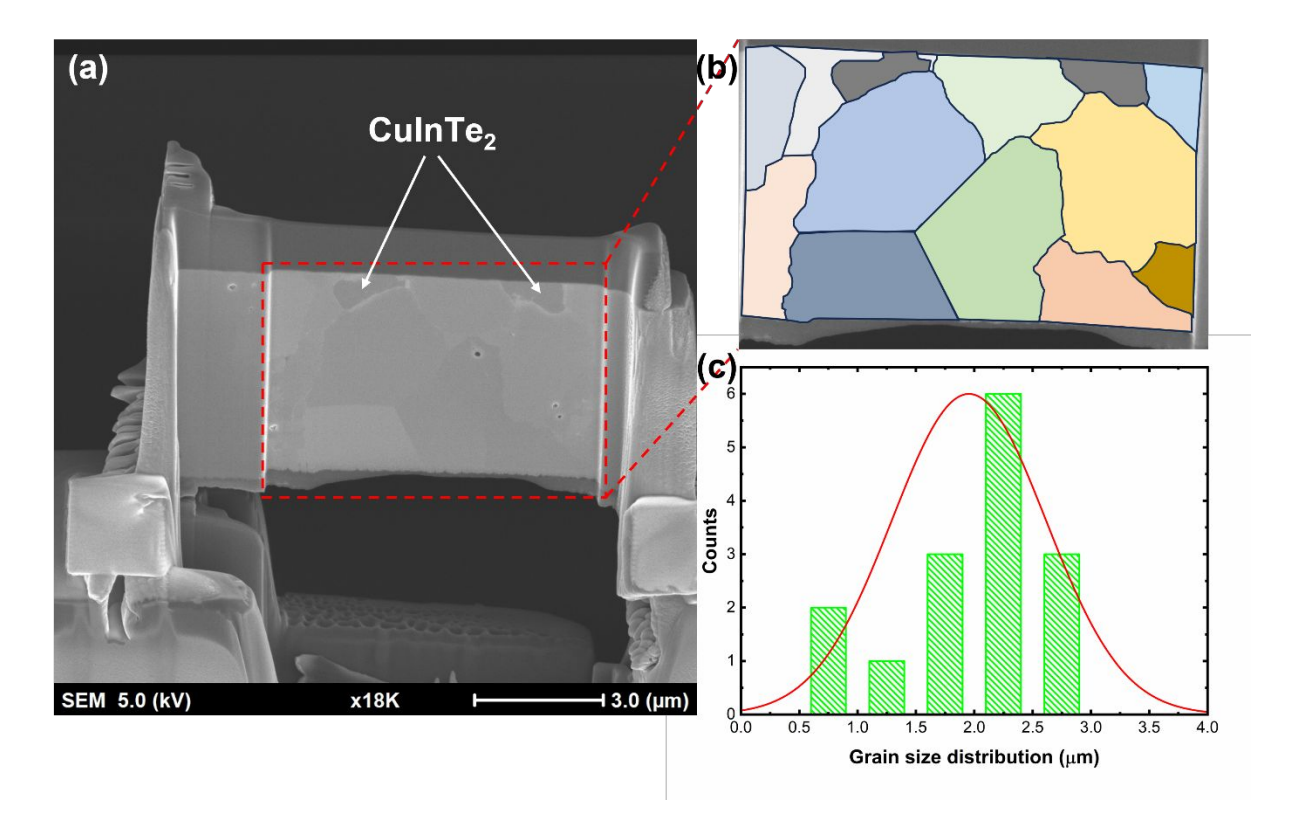


Figure S13. (a) SEM image of the FIB sample during the lifting process, (b) Schematic illustration of the grains seen in the FIB sample and (c) average grain size in the FIB sample.

Band gap approximation

The band gap for all the compositions was approximated using the Goldsmid-Sharp equation S1,8 where e is the charge of an electron, T_{max} is the the temperature at which the maximum experimental Seebcek coefficient, S_{max} occurs. A summary of the calculation is given in Table S1 below.

$$E_g = 2eS_{max}T_{max} \tag{S1}$$

Table S1. Summary of band gap calculation.

| Composition | S_{max} (V K ⁻¹) | $T_{max}(\mathbf{K})$ | $E_g(eV)$ |
|-------------|--------------------------------|-----------------------|-----------|
| x=0.00 | 1.10×10^{-4} | 823 | 0.1813 |
| x=0.01 | 1.50×10^{-4} | 823 | 0.2473 |
| x=0.02 | 1.58×10^{-4} | 773 | 0.2443 |
| x=0.03 | 1.57×10^{-4} | 773 | 0.2431 |
| x=0.04 | 1.52×10^{-4} | 723 | 0.2203 |

Debye-Callaway model

According to the Debye-Callaway model,⁹ the lattice thermal conductivity is computed in the flowing way.

$$\kappa_{lat} = \frac{k_B}{2\pi^2 \nu} \left(\frac{k_B T}{\hbar}\right)^3 \int_0^{\theta_D/T} \tau_{tot}(x) \frac{x^4 \exp(x)}{\left[\exp(x) - 1\right]^2} dx \tag{S2}$$

The integrand item of the equation above is the spectral lattice thermal conductivity, κ_s which is calculated as below.^{10–12}

$$\kappa_{s} = \frac{k_{B}}{2\pi^{2}\nu} \left(\frac{k_{B}T}{\hbar}\right)^{3} \tau_{tot}(x) \frac{x^{4} \exp(x)}{\left[\exp(x) - 1\right]^{2}} dx \tag{S3}$$

In the above equations, x is a dimensionless variable given by $x = \hbar \omega / k_B T$ where ω is the phonon frequency. θ_D is the Debye temperature which is calculated using $k_B \theta_D = \hbar \nu (6\pi^2 N)^{1/3}$

where N is the number of atoms per volume and v is the average sound velocity. 12,13 τ_{tot} is the combined relaxation time obtained after considering relaxation times due to the Umklapp process (U), Normal process (N), grain boundary scattering (GB), point defect scattering (PD), and nanoprecipitates scattering (NP). This is represented by Matthiessen's rule below.

$$\tau_{tot} = \left(\tau_U^{-1} + \tau_N^{-1} + \tau_{GB}^{-1} + \tau_{PD}^{-1} + \tau_{NP}^{-1}\right)^{-1} \tag{S4}$$

Specific relaxation times are determined as described below.

Umklapp process: 10,12

$$\tau_U^{-1} = \frac{\hbar \gamma^2 x^2 T}{M_{atom} v^2 \theta_D} \left(\frac{k_B T}{\hbar}\right)^2 exp\left(-\frac{\theta_D}{3T}\right) \tag{S5}$$

Where k_B,\hbar,γ,T , and M_{atom} are the Boltzmann constant, reduced Planck constant, Grüneisen parameter, ¹⁰ absolute temperature (300 K), and average atomic mass, respectively.

Normal process: 10,12

$$\tau_N^{-1} = \beta \tau_U^{-1} \tag{S6}$$

Where β is the ratio of Umklapp scattering to Normal phonon scattering.¹⁰

Grain boundary scattering: 10,12

$$\tau_{GB}^{-1} = \frac{\nu}{L} \tag{S7}$$

Where L is the average grain size taken from SEM images as shown in Figure S13.

Point defect scattering:14

$$\tau_{PD}^{-1} = \frac{V_{atom}\omega^4}{4\pi\nu^3} \sum_{i} x_i \left[\left(\frac{M_i - M}{M} \right)^2 + \varepsilon \left(\frac{r_i - r}{r} \right)^2 \right]$$
 (S8)

Where V_{atom} is the average atomic volume, x_i is the mole fraction of i^{th} cation at the Sn sublattice, M_i and M are the molar mass of i^{th} cation and Sn, r_i and r are the radius of the i^{th} cation and Sn and ε is the phenomenological parameter obtained from the literature.¹⁵ Nanoprecipitates scattering:16

$$\tau^{-1} = v \left[(2\pi R^2)^{-1} + \left(\pi R^2 \frac{4}{9} \left(\frac{\Delta D}{D} \right)^2 \left(\frac{\omega R}{v} \right)^4 \right)^{-1} \right]^{-1} N_p$$
 (S9)

Where R is the average radius of the precipitates, ΔD is the difference in density between the matrix and precipitates, D is the density of the matrix and N_p is the number density of the precipitates.

Table S2. Input parameters used in the Debye-Callaway model.

| Input parameter | Value |
|---|-------------------------|
| Debye temperature, θ_D (K) | 169.40 |
| Average sound velocity, $v \text{ (m s}^{-1})$ | 1800 ^{12,13} |
| Grüneisen parameter, γ | 2.210 |
| Average atomic mass, M (Kg) | 2.05×10^{-25} |
| Average atomic volume, V_{atom} (m ³) | 3.17×10^{-29} |
| Ratio of Umklapp scattering to Normal phonon scattering, β | 1.810 |
| Average grain size, L (m) | 1.95 × 10 ⁻⁶ |
| Phenomenological parameter, ε | 8315 |
| Density of the matrix (SnTe, g cm ⁻³) | 6.457 |
| Density of the precipitates (CuInTe ₂ , g cm ⁻³) | 6.043 |
| Average radius of precipitates, R (m) | 6.5 × 10 ⁻⁷ |
| Number density of precipitates, N_p (m ⁻³) | 7.0×10^{18} |

REFERENCES

- (1) Wang, X.; Yao, H.; Zhang, Z.; Li, X.; Chen, C.; Yin, L.; Hu, K.; Yan, Y.; Li, Z.; Yu, B.; Cao, F.; Liu, X.; Lin, X.; Zhang, Q. Enhanced Thermoelectric Performance in High Entropy Alloys Sn_{0.25}Pb_{0.25}Mn_{0.25}Ge_{0.25}Te. ACS Appl. Mater. Interfaces 2021, 13 (16), 18638–18647.
- (2) Hu, L.; Zhang, Y.; Wu, H.; Li, J.; Li, Y.; Mckenna, M.; He, J.; Liu, F.; Pennycook, S. J.; Zeng, X. Entropy Engineering of SnTe: Multi-Principal-Element Alloying Leading to Ultralow Lattice Thermal Conductivity and State-of-the-Art Thermoelectric Performance. Adv. Energy Mater. 2018, 8 (29), 1802116.
- (3) Zhang, Q.; Guo, Z.; Wang, R.; Tan, X.; Song, K.; Sun, P.; Hu, H.; Cui, C.; Liu, G.; Jiang, J. High-Performance Thermoelectric Material and Module Driven by Medium-Entropy Engineering in SnTe. Adv. Funct. Mater. 2022, 32 (35), 2205458.
- (4) Zhou, Y. M.; Wu, H. J.; Pei, Y. L.; Chang, C.; Xiao, Y.; Zhang, X.; Gong, S. K.; He, J. Q.; Zhao, L.-D. Strategy to Optimize the Overall Thermoelectric Properties of SnTe via Compositing with Its Property-Counter CuInTe₂. *Acta Mater.* 2017, 125, 542–549.
- (5) Hwang, J.; Lee, M.; Yu, B. K.; Han, M. K.; Kim, W.; Kim, J.; Al Rahal Al Orabi, R.; Wang, H.; Acharya, S.; Kim, J.; Jin, Y.; Park, H.; Kim, S.; Yang, S. H.; Kim, S. J. Enhancement of Thermoelectric Performance in a Non-Toxic CuInTe₂/SnTe Coated Grain Nanocomposite. *J. Mater. Chem. A* **2021**, *9* (26), 14851–14858.
- (6) Hÿtch, M. J.; Snoeck, E.; Kilaas, R. Quantitative Measurement of Displacement and Strain Fields from HREM Micrographs. *Ultramicroscopy* **1998**, *74* (3), 131–146.
- (7) Kim, H.; Kihoi, S. K.; Lee, H. S. Point Defects Control in Non-Stoichiometric CuInTe₂
 Compounds and Its Corresponding Effects on the Microstructure and Thermoelectric
 Properties. J. Alloys Compd. 2021, 869, 159381.
- (8) Goldsmid, H. J.; Sharp, J. W. Estimation of the Thermal Band Gap of a Semiconductor

- from Seebeck Measurements. J. Electron. Mater. 1999, 28 (7), 869–872.
- (9) Callaway, J.; Von Baeyer, H. C. Effect of Point Imperfections on Lattice Thermal Conductivity. *Phys. Rev.* **1960**, *120* (4), 1149–1154.
- (10) Yang, Q.; Lyu, T.; Nan, B.; Dong, Y.; Tie, J.; Xu, G. Locally Ordered Nano-Domains as Novel Microstructure Defects Suppressing the Phonon Transport in SnTe Thermoelectrics. *J. Eur. Ceram. Soc.* **2022**, *42* (3), 1001–1006.
- (11) Moshwan, R.; Liu, W. Di; Shi, X. L.; Wang, Y. P.; Zou, J.; Chen, Z. G. Realizing High Thermoelectric Properties of SnTe via Synergistic Band Engineering and Structure Engineering. *Nano Energy* **2019**, *65*, 104056.
- (12) Lyu, T.; Yang, Q.; Meng, F.; He, J.; Benton, A.; Chronister, C.; Li, Z.; Xu, G. Enhancing Thermoelectric Performance of Sn_{1-x}Sb_{2x/3}Te via Synergistic Charge Balanced Compensation Doping. *Chem. Eng. J.* **2021**, *404*, 126925.
- (13) Banik, A.; Vishal, B.; Perumal, S.; Datta, R.; Biswas, K. The Origin of Low Thermal Conductivity in Sn_{1-x}Sb_xTe: Phonon Scattering via Layered Intergrowth Nanostructures. *Energy Environ. Sci.* **2016**, *9* (6), 2011–2019.
- (14) Yan, X.; Zheng, S.; Zhou, Z.; Wu, H.; Zhang, B.; Huang, Y.; Lu, X.; Han, G.; Wang, G.; Zhou, X. Melt-Spun Sn_{1-x-y}Sb_xMn_yTe with Unique Multiscale Microstructures Approaching Exceptional Average Thermoelectric ZT. *Nano Energy* 2021, 84, 105879.
- (15) Guo, F.; Cui, B.; Liu, Y.; Meng, X.; Cao, J.; Zhang, Y.; He, R.; Liu, W.; Wu, H.; Pennycook, S. J.; Cai, W.; Sui, J. Thermoelectric SnTe with Band Convergence, Dense Dislocations, and Interstitials through Sn Self-Compensation and Mn Alloying. *Small* 2018, 14 (37), 1802615.
- (16) Sun, Q.; Chen, Z. Y.; Li, M.; Shi, X. L.; Xu, S. D.; Yin, Y.; Dargusch, M.; Zou, J.; Ang, R.; Chen, Z. G. Structural Evolution of High-Performance Mn-Alloyed Thermoelectric Materials: A Case Study of SnTe. *Small* 2021, *17* (25), 2100525.